Composition-Engineered Intrinsic Stability in 2D Perovskite Optoelectronic Synapses for Neuromorphic Vision

Honglai Li[1†,*], Wei Li[1†], Herong Sheng[4,6†], Changhao Liu[1], Wenjun Yang[1], Jinpeng Zhao[5], Shida Feng[1], Biyuan Zheng[3], Chenglin He[3], Jiahuan Ren[1], Liang Ma[5], Tingzhao Fu[3], Chun Zhao[4], Yuxiao Fang[4*], Weihao Zheng[3*], Dong Li[2], Zhihong Zhu[3], Anlian Pan[2,7*]

1 College of Physics Science and Technology, Hebei University, Baoding 071002, China.
2 Hunan Institute of Optoelectronic Integration, College of Materials Science and Engineering, Hunan University, Changsha 410082, China.
3 College of Advanced Interdisciplinary Studies & Hunan Provincial Key Laboratory of Novel Nano-Optoelectronic Information Materials and Devices, National University of Defense Technology, Changsha 410073, China.
4 School of Advanced Technology, Xi'an Jiaotong-Liverpool University, Suzhou 215123, China.
5 College of Physics and Electronic Engineering, Hengyang Normal University, Hengyang 421008, China.
6 Department of Electrical Engineering and Electronics, University of Liverpool, Liverpool L69 3BX, UK.
7 School of Physics and Electronics, Hunan Normal University, Changsha, Hunan, 410081, China.
† These authors contributed equally: Honglai Li, Wei Li, Herong Sheng.

Email: anlian.pan@hnu.edu.cn; zhengweihao@nudt.edu.cn; yuxiao.fang02@xjtlu.edu.cn; lihonglai@hnu.edu.cn

ABSTRACT

Operational instability remains a key obstacle for halide perovskites in neuromorphic optoelectronics, where sustained and reproducible photoresponses are required for in-sensor computing. Here we report vapor-phase growth of composition-tunable two-dimensional (2D) inorganic perovskites, $Cs_xRb_{1-x}PbBr_3$ ($0 \leqslant x \leqslant 1$), and show that A-site cation alloying provides an effective route to simultaneously improve optical performance and structural robustness. By mapping the full Cs-Rb compositional space, we identify a narrow intermediate regime ($x \approx 0.8$) where lattice strain is minimized and defect formation is suppressed. Perovskites in this regime exhibit substantially enhanced resistance to moisture, thermal stress, and ion migration compared with either end member. These stability gains translate directly to device operation, enabling broadband photodetectors with fast response, high reproducibility, and long-term durability. Using the optimized $Cs_{0.81}Rb_{0.19}PbBr_3$ composition, we further demonstrate optoelectronic synaptic devices that reproduce key synaptic functions, including paired-pulse facilitation (PPF) and light-programmable synaptic weights. Integrated into a spiking neural network (SNN), the devices enable real-time fire detection with 85% accuracy while maintaining stable performance over seven days. This work establishes composition-engineered 2D inorganic perovskites as a robust platform for neuromorphic vision and energy-efficient in-sensor computing.

Keywords: stability, perovskite, synapse, neuromorphic vision

INTRODUCTION

Neuromorphic optoelectronic systems aim to mimic biological perception by integrating sensing, memory, and computation into a single hardware framework (1-7). Achieving this functionality requires semiconductor materials that combine strong light-matter interaction, tunable optoelectronic properties, and long-term operational stability under continuous optical and electrical stimuli (8-9). Two-dimensional (2D) semiconductors are attractive in this context because their reduced dimensionality can mitigate defect formation and facilitate heterogeneous integration (10-11). Yet, identifying material platforms that deliver both high performance and reliable stability for neuromorphic vision remains challenging.

Metal halide perovskites have emerged as promising candidates due to their high absorption coefficients (12), defect tolerance (13), and compositionally tunable bandgaps (14), enabling photodetectors, light-emitting devices, and lasers (15-20). All-inorganic perovskites are particularly appealing because they avoid volatile organic components and typically show improved thermal and environmental stability compared with hybrid analogues (21-22). However, even fully inorganic perovskites are still vulnerable to phase instability, lattice distortion, and ion migration, especially under prolonged illumination, elevated temperature, and

ambient exposure (23,24). These degradation pathways fundamentally limit their suitability for neuromorphic applications, which demand persistent and reproducible photoresponses over extended operation.

A-site cation engineering has proven effective for improving perovskite stability and tuning electronic structure (25). Partial substitution of Cs^+ with smaller alkali cations such as Rb^+, K^+, or Na^+ can relieve lattice strain, suppress unfavorable phase transitions, and reduce defect densities (26-28). Although A-site alloying has improved stability and device performance in bulk and thin-film perovskites (29), a systematic understanding of how continuous compositional tuning governs the structural robustness and optoelectronic functionality of 2D inorganic perovskites—and how these effects translate into neuromorphic device performance—remains limited.

Here we demonstrate vapor-phase growth of fully composition-tunable 2D $Cs_xRb_{1-x}PbBr_3$ perovskites ($0 \le x \le 1$), enabling precise control over A-site cation ratios across the entire alloy range. By correlating composition with crystal structure, optical properties, and environmental stability, we identify an optimal intermediate alloy, $Cs_{0.81}Rb_{0.19}PbBr_3$, that exhibits strong resistance to moisture, thermal stress, and ion migration. Building on this stability-optimized platform, we realize broadband photodetectors and optoelectronic synapses that reproduce key synaptic behaviors. Finally, integration into a spiking neural network enables real-time fire detection with 85% accuracy and negligible degradation over one week. These results highlight compositionally engineered 2D inorganic perovskites as a viable materials basis for robust neuromorphic vision and energy-efficient in-sensor computing.

RESULTS

Single-crystalline $Cs_xRb_{1-x}PbBr_3$ ($0 \le x \le 1$) nanosheets were directly grown on freshly exfoliated mica (001) substrates by vapor-phase deposition, yielding large-area two-dimensional crystals with uniform composition across the full alloy range (Figs. 1a-c). To accommodate the distinct volatility and reaction kinetics of different A-site ratios, the growth temperature was adjusted from 350 to 500℃ (see Experimental Section). As illustrated in Fig. 1a, the alloyed perovskite adopts a quasi-rectangular 2D lattice consisting of corner-sharing $[PbBr_6]^{4-}$ octahedra extending along the a- and c-axes, while Cs^+ and Rb^+ occupy the cuboctahedral A-sites. Replacing Cs^+ (1.67 Å) with the smaller Rb^+ (1.48 Å) is expected to contract the lattice and induce subtle octahedral tilting, leading to a gradual structural distortion of the 2D framework (30-32). Across all compositions, the nanosheets exhibit well-defined rectangular morphologies with lateral sizes up to ~128 μm and thickness down to a few nanometers, consistent with strongly anisotropic layer-by-layer growth (Fig. 1c). AFM and SEM analyses further reveal smooth surfaces and excellent thickness uniformity, with the thinnest nanosheets

reaching ~7.61 nm (Fig. 1d and Figs. S1,2). Elemental mapping confirms that both end members ($CsPbBr_3$ and $RbPbBr_3$) and intermediate alloys maintain homogeneous elemental distributions without detectable compositional fluctuation (Figs. S4-5), indicating reliable stoichiometric control during vapor growth. X-ray diffraction (XRD) patterns show a systematic evolution of lattice parameters with increasing Rb incorporation (Fig. 1e). Both $CsPbBr_3$ and $RbPbBr_3$ nanosheets match their reference patterns and exhibit a monoclinic phase at room temperature. Diffraction peaks at ~15.4°, 21.7°, and 30.6° can be indexed to the (001), (011), and (002) planes, respectively, while the pronounced (200) reflection suggests preferential in-plane crystal growth. Notably, all Bragg peaks shift monotonically toward higher angles as the Rb fraction increases, consistent with lattice contraction induced by substitution of larger Cs^+ ions with smaller Rb^+ ions (33). No additional peaks or splitting are observed throughout the entire composition range, indicating single-phase solid-solution formation without phase segregation. X-ray photoelectron spectroscopy (XPS) provides further evidence of successful A-site alloying (Fig. 1f) (34). The relative intensities of Cs 3d and Rb 3d signals evolve monotonically with composition, accompanied by small binding-energy shifts that reflect changes in the local A-site chemical environment. In contrast, the Pb 4f and Br 3d spectra remain nearly unchanged (Fig. S3), suggesting that alloying primarily modifies the A-site sublattice while preserving the integrity of the $[PbBr_6]^{4-}$ framework.

Atomic-resolution HAADF-STEM was used to directly examine the structural quality and compositional uniformity of the alloyed nanosheets (Fig. 2). Low-magnification HAADF-STEM imaging shows atomically flat surfaces and well-defined edges, consistent with high-quality single-crystalline growth (Fig. 2a). The corresponding SAED pattern exhibits sharp diffraction spots (Fig. 2b and Fig. S6), confirming long-range crystallographic order. For the $Cs_{0.45}Rb_{0.55}PbBr_3$ alloy, lattice spacings measured along the (100) and (001) directions are 0.576 and 0.583 nm, respectively, both smaller than those of pristine $CsPbBr_3$, consistent with the expected lattice contraction upon Rb incorporation. EDS mapping acquired from the region marked in Fig. 2a shows a uniform distribution of Cs, Rb, Pb, and Br across the nanosheet (Fig. 2c), and the corresponding spectrum confirms the intended stoichiometry (Fig. 2d).

Figure 2e shows an atomic-resolution HAADF-STEM image of $Cs_{0.81}Rb_{0.19}PbBr_3$ viewed along the (001) zone axis. The contrast is dominated by the projected $[PbBr_6]^{4-}$ octahedral framework, while the A-site sublattice exhibits intensity variations consistent with mixed Cs/Rb occupancy. Importantly, no contrast modulation or domain-like features are observed, suggesting random alloying rather than nanoscale phase separation. The experimental image agrees well with the simulated structure (inset), supporting the structural assignment. FFT analysis reveals well-defined diffraction spots with high symmetry (Fig. 2f), further indicating single crystallinity. Atomic-resolution EDS mapping resolves the spatial distribution of Cs and Pb (Fig. 2g), and the measured lattice spacings along the (100) and (001)

directions are 0.581 and 0.586 nm, respectively (Fig. 2h), consistent with the composition-dependent lattice evolution. Similar results were obtained for $Cs_{0.72}Rb_{0.28}PbBr_3$ (Fig. S7), confirming that phase purity and alloy homogeneity are preserved across different Cs/Rb ratios. Together, these results establish that continuous A-site alloying enables systematic lattice modulation in 2D $Cs_xRb_{1-x}PbBr_3$ nanosheets without compromising crystalline integrity.

The optical properties of $Cs_xRb_{1-x}PbBr_3$ ($0 \le x \le 1$) nanosheets can be continuously tuned through A-site composition. Increasing the Rb fraction results in a monotonic blue shift of the photoluminescence (PL) peak from 525 nm for $CsPbBr_3$ ($x = 1$) to 447 nm for $RbPbBr_3$ ($x = 0$), covering the full blue-to-green spectral range (Fig. 3a). All spectra remain narrow and symmetric, indicating that alloying does not introduce significant inhomogeneous broadening or strong defect-related emission. Bandgap arrangement of the alloys (Fig. S8) show that substituting Cs with Rb increases the bandgap by widening the separation between the conduction-band minimum and valence-band maximum, consistent with the experimentally observed PL evolution (35). This agreement indicates that A-site alloying provides a direct and reliable route to bandgap engineering in 2D inorganic perovskites. Under 400 nm femtosecond pulsed excitation, all compositions exhibit stimulated emission with composition-tunable lasing wavelengths (Fig. 3b and Fig. S9). The emission intensity as a function of excitation power shows the characteristic threshold behavior expected for lasing (Fig. S10). Rate-equation analysis was applied to quantify the lasing dynamics (Supporting Information Note S1) (36-40). The extracted lasing thresholds and spontaneous emission coupling factors (β) remain comparable across the Cs-Rb range (Fig. 3c), suggesting that optical gain and cavity quality are largely maintained despite the composition-driven lattice contraction.

Time-resolved photoluminescence (TRPL) measurements further reveal that carrier recombination dynamics are only weakly dependent on composition. Below threshold, all nanosheets exhibit nanosecond-scale decay dominated by spontaneous recombination, whereas above threshold the lifetime collapses into the picosecond regime due to stimulated emission. Figures 3d and 3e show representative streak-camera images of a $Cs_{0.5}Rb_{0.5}PbBr_3$ nanosheet recorded at 0.8 Pth and 1.5 Pth, respectively, with similar behavior observed for other compositions (Figs. S11-14). The transition from spontaneous to stimulated emission is accompanied by a sharp acceleration of decay kinetics. Figure 3g plots the excited-state decay curves of $Cs_{0.5}Rb_{0.5}PbBr_3$ nanosheet under 0.8 Pth and 1.5 Pth excitation intensities, respectively. Further, the two time-resolved fluorescence curves underwent exponential decay fitting, including deconvolution of the instrumental response curve. The PL decay curves were fitted using a multi-exponential model accounting for instrumental response, as follows (41):

$$N(t) \propto I(t) = \sum A_i \exp\left(-\frac{t}{\tau_i}\right) \qquad (1)$$

Here, $N(t)$ is the total carrier density at delay time t, which is proportional to the fluorescence intensity $I(t)$. A_i (i = 1, 2, and 3) are the weight percentages, representing the carrier density contribution of different lifetime components. τ_i (i = 1, 2, and 3) are the decay time constants. The fitting results are summarized in Table S1. For all compositions, the effective lifetime decreases from ~5.3 ns below threshold to ~6.7 ps above threshold. Importantly, the extracted spontaneous and stimulated recombination components show minimal variation with composition (Figs. 3f-h), indicating that A-site alloying primarily tunes the band structure while introducing little additional non-radiative loss.

To assess device-level performance, individual photodetectors were fabricated by transferring Au electrodes onto single $Cs_xRb_{1-x}PbBr_3$ nanosheets, defining a channel length of 5 μm (Fig. 4a). Under 405 nm illumination, the photocurrent shows a pronounced dependence on A-site composition (Fig. 4b). As the Rb fraction increases, the photocurrent decreases from 41.6 nA for $CsPbBr_3$ to 0.31 nA for $RbPbBr_3$. This trend is consistent with the stronger lattice contraction and strain introduced by Rb incorporation, which can enhance carrier scattering and reduce transport efficiency. Responsivity (R) and external quantum efficiency (EQE) were extracted using Equations (2) and (3):

$$R=\frac{I_{ph}-I_d}{PS} \qquad (2)$$

where I_{ph}, I_d, $P$and S, represent the photocurrent, dark current, optical irradiance, active area (100 μm^2), respectively (42). EQE (%) is positively correlated with responsivity (R) and is defined by the equation:

$$E=\frac{Rhc}{e\lambda} \qquad (3)$$

where h, c, e, and λ denote Planck's constant ($h \approx 6.63 \times 10^{-34}$ J·s), the speed of light ($c \approx 3 \times 10^8$ m/s), the electron charge ($e \approx 1.602 \times 10^{-19}$ C), and the wavelength of incident light, respectively (43). As summarized in Fig. 4c, both R and EQE increase monotonically with Cs content. At an illumination intensity of 3.936 3.936 mW/cm^2, R increases from 0.23 A/W ($RbPbBr_3$) to 10.37 A/W ($CsPbBr_3$), while EQE rises from 0.71% to 31.78%. Spectral response measurements reveal broadband sensitivity spanning 375-520 nm. For the $Cs_{0.48}Rb_{0.52}PbBr_3$ device, the responsivity reaches a maximum of 9.41 A W^{-1} at ~460 nm (Figs. 4d,e), consistent with its optical bandgap. The peak sensitivity wavelength can be continuously tuned with composition (inset of Fig. 4e), reflecting the bandgap modulation enabled by A-site alloying. In addition to its spectral tunability, the $Cs_{0.48}Rb_{0.52}PbBr_3$ photodetector exhibits fast transient response, with a rise time of ~0.2 ms and a fall time of ~1.615 ms (Fig. 4f). The device maintains stable switching behavior up to modulation frequencies of 100 Hz without significant distortion (Fig. 4g), and shows reproducible photocurrent

responses under periodic illumination at different wavelengths (Fig. 4h). Comparable trends were observed for other compositions (Figs. S15-23).

While high responsivity is important, neuromorphic vision systems place an equally stringent requirement on operational stability. We therefore systematically evaluated environmental, thermal, and optical stability across the entire Cs-Rb compositional range. Notably, a pronounced stability maximum emerges in a narrow intermediate regime near x ≈ 0.8. Under continuous illumination at 30% relative humidity, devices based on intermediate alloys retain photocurrent far more effectively than either end member (Fig. 4i and Fig. S24). Among all compositions, $Cs_{0.81}Rb_{0.19}PbBr_3$ shows the highest photocurrent retention, followed by x = 0.62, 0.48, and 0.24, whereas $CsPbBr_3$ and $RbPbBr_3$ degrade most rapidly. This stability hierarchy remains consistent during long-term storage in ambient air (27 °C, 30% RH) (Fig. 4j) and under thermal stress up to 380 K (Figs. S25,26), indicating that the enhanced durability is intrinsic to the optimized alloy composition rather than a measurement artifact. Optical stability was further evaluated by monitoring PL intensity. To isolate intrinsic lattice stability from moisture- and oxygen-induced degradation, nanosheets were encapsulated with a PMMA layer (44,45) during PL measurements (Figs. 4k,l). Under continuous excitation and prolonged storage, $Cs_{0.81}Rb_{0.19}PbBr_3$ exhibits minimal PL quenching, whereas both end members show pronounced intensity loss. The consistent trends observed in electrical stability (photocurrent retention) and optical stability (PL retention) suggest that moderate Rb incorporation effectively suppresses defect formation and ion migration while avoiding the excessive lattice distortion present at high Rb fractions. Together, these results define a narrow and well-resolved compositional window where lattice strain is optimally balanced, yielding improved structural robustness without compromising optoelectronic function. This intrinsic stability advantage provides a key materials basis for the neuromorphic devices discussed below. For subsequent synaptic measurements, the same PMMA encapsulation strategy was employed to minimize direct exposure to ambient oxygen and moisture.

Reliable neuromorphic operation requires synaptic plasticity that remains reproducible under repeated stimulation and external perturbations. Guided by the compositional stability analysis above, $Cs_{0.81}Rb_{0.19}PbBr_3$ was selected as the representative platform for optoelectronic synapse demonstrations. The resulting photosynaptic device integrates light sensing and memory within a single architecture (Fig. 5a), enabling direct conversion of optical stimuli into synaptic weight modulation. To enhance synaptic plasticity, a 20 nm HfO_2 charge-trapping layer was introduced, enabling persistent modulation of the channel conductance through photogenerated carrier trapping (46). Under paired optical pulses, the device exhibits a clear paired-pulse facilitation (PPF) effect, a hallmark of short-term synaptic plasticity (Fig. 5b and Figs. S28,29). The PPF index decreases monotonically with increasing pulse interval and can be well fitted by a double-

exponential decay, indicating the coexistence of fast and slow relaxation processes. The temporal evolution of the PPF index follows (47):

$$PPF=C_1\exp(-\frac{\Delta t}{\tau_1})+C_2\exp(-\frac{\Delta t}{\tau_2}) \quad (4)$$

where C_1 and C_2 denote the initial facilitation amplitudes, and τ_1 and τ_2 correspond to fast and slow relaxation time constants, respectively, demonstrating the potential of PPF in visual systems. These dynamics are attributed to delayed recombination and gradual release of carriers trapped at surface and interfacial states. Beyond short-term plasticity, the synaptic response can be continuously tuned by the temporal profile of the optical stimulus. Increasing either pulse width or pulse frequency produces a monotonic increase in excitatory postsynaptic current (EPSC) (Figs. 5c,d and Fig. S30), consistent with cumulative carrier trapping and incomplete relaxation between successive pulses. Such pulse-dependent behavior closely resembles learning processes in biological synapses.

Electrical gating provides an additional handle to modulate synaptic weight. As the back-gate voltage is swept toward more negative values, both the switching window and EPSC amplitude increase systematically (Figs. 5e,f and Fig. S31), enabling programmable adjustment of synaptic response without altering the optical stimulus conditions (48). Wavelength-dependent measurements further show that synaptic potentiation correlates strongly with the intrinsic absorption profile of the alloy (Fig. 5g). Optical excitation at 477 nm produces the strongest EPSC response, followed by 520 nm and 427 nm illumination, consistent with the spectral responsivity of the photodetector devices. The EPSC also increases monotonically with pulse number, enabling gradual and analog-like weight updates that are essential for neuromorphic learning.

Importantly, the synaptic behavior remains robust under thermal stress. Although the peak current decreases gradually with increasing temperature, the switching characteristics and plasticity behavior are preserved up to 380 K (Fig. 5h). This thermal tolerance is consistent with the enhanced lattice stability and suppressed ion migration observed for $Cs_{0.81}Rb_{0.19}PbBr_3$. Device reliability was further evaluated through endurance and shelf-life tests. After more than 100 optical stimulation cycles, the device shows negligible degradation in switching behavior (Fig. 5i), and stable synaptic responses are retained after storage in ambient air for seven days (Fig. 5j). Finally, the device is capable of emulating higher-order learning behavior, including a learning-forgetting-relearning process (Fig. 5k), where fewer stimuli are required to restore synaptic weights after partial memory decay. The reproducibility of these behaviors highlights that intrinsic materials stability directly translates into synaptic fidelity, providing a practical foundation for robust neuromorphic optoelectronic hardware. Collectively, the device exhibits stable and tunable synaptic plasticity across a wide range of optical conditions, including pulse-width dependence, frequency dependence, power dependence

(Fig. S32), wavelength dependence, and both short-term and long-term plasticity. Building on these device-level characteristics, we next integrate the optoelectronic synapse into neural network models to evaluate system-level in-sensor computing performance.

To examine whether the stability advantages at the materials and device levels can translate into reliable system-level computation, we implemented a spiking neural network (SNN) for visual classification using experimentally measured characteristics of the $Cs_{0.81}Rb_{0.19}PbBr_3$ photosynaptic devices (Fig. 6a). Rather than pursuing the highest possible algorithmic accuracy, our goal is to assess whether stable perovskite-based synapses can support consistent spiking computation without requiring frequent recalibration. The network adopts a ResNet-inspired SNN architecture, where convolutional layers extract spatial features and leaky integrate-and-fire (LIF) neurons encode temporal information through spike trains. By means of simulation, the electrical conductance of the memristor is mapped to the weights of the network [16] (Review3, Q5). We first evaluated the trainability of the device-informed SNN on the FashionMNIST dataset (Fig. S33). As shown in Fig. 6b, both training and inference accuracies increase rapidly during early epochs and converge to stable values close to 90%, with only a small gap between training and test performance. The corresponding confusion matrix (Fig. 6c) exhibits strong diagonal dominance, indicating reliable discrimination among classes. Similar convergence behavior is observed for the MNIST dataset (Figs. S35,36), suggesting that the network generalizes well and does not suffer from noticeable overfitting. In addition, firing statistics of LIF neurons remain well regulated across layers throughout training (Fig. 6d and Figs. S37,38,40), avoiding both excessive spiking activity and neuronal silence. These results indicate that the ResNet-SNN architecture provides stable temporal dynamics compatible with device-level implementation. It should be emphasized that the fire-detection task presented here serves as a proof-of-concept system-level validation of the compatibility between the stable $Cs_{0.81}Rb_{0.19}PbBr_3$ photosynaptic device and the ResNet-SNN computational framework, rather than a fully deployed fire-detection system. The objective is to evaluate whether experimentally measured synaptic dynamics can support stable neuromorphic inference. Practical deployment would require further development of large-scale device arrays, peripheral circuits, real-time image acquisition, extended environmental reliability tests, and system-level power evaluation (Review3, Q4).

Having established network convergence on benchmark datasets, we next evaluated performance on a more application-relevant fire detection task based on RGB image sequences. Compared with digit datasets, fire scenes exhibit substantially higher complexity due to background clutter, illumination variation, and diverse flame morphologies. Despite these challenges, the device-informed SNN reaches an inference accuracy of ~85% after ~30 epochs (Fig. 6e). The confusion matrix (Fig. 6f) shows that 90.41% of fire images (2,065 samples) are

correctly classified, while 19.93% of non-fire images (1,536 samples) are misclassified as fire, demonstrating balanced classification behavior under realistic visual complexity.

Long-term inference stability is particularly critical for safety-related deployment. To evaluate temporal robustness, we monitored fire-recognition accuracy over an extended period. As shown in Fig. 6g, the inference accuracy varies by less than 1% over one week, consistent with the suppressed conductance drift observed in $Cs_{0.81}Rb_{0.19}PbBr_3$ synaptic devices (Fig. S42). This result indicates that the stability engineered at the materials level can directly propagate to system-level neuromorphic computation, enabling consistent inference performance without retraining or recalibration. Beyond the demonstrated fire-detection task, the proposed stability-driven photosynaptic platform may be extended to broader application scenarios requiring reliable and energy-efficient visual perception. For autonomous driving systems, stable perovskite photosynapses could be used for event-driven hazard perception, early fire or smoke warning, and low-latency optical signal preprocessing under complex illumination conditions. For robot vision, the integration of light sensing, memory, and synaptic weight modulation within a single device could enable adaptive environmental recognition and edge visual intelligence with reduced data-transfer overhead. The long-term stability demonstrated in this work is particularly important for these application scenarios, because practical neuromorphic vision systems require not only high instantaneous accuracy but also stable inference without frequent recalibration or retraining.

CONCLUSIONS

In summary, we demonstrate that compositional engineering of 2D inorganic perovskites provides a practical route toward stable neuromorphic optoelectronic systems. By continuously tuning the A-site composition in $Cs_xRb_{1-x}PbBr_3$ nanosheets, we identify a narrow intermediate regime in which lattice strain is minimized and defect-related degradation is suppressed. The optimized $Cs_{0.81}Rb_{0.19}PbBr_3$ composition exhibits enhanced resistance to moisture, thermal stress, and ion migration, enabling stable photodetection and reproducible synaptic plasticity. Beyond device demonstrations, we further show that experimentally measured synaptic responses can be directly incorporated into spiking neural networks to support system-level neuromorphic vision. The resulting ResNet-SNN achieves stable training convergence and enables real-time fire detection with ~85% accuracy, while maintaining performance fluctuations below 1% over one week of operation. These results establish a clear materials-device-algorithm connection, highlighting that intrinsic material stability is a key requirement for reliable in-sensor computing. More broadly, this work suggests that stability-driven compositional design offers an effective strategy to bridge emerging perovskite materials with practical neuromorphic hardware, where long-term operational consistency is as important as instantaneous performance.

Acknowledgments

This work was supported by the National Key Research and Development Program of China (No. 2022YFA1204300), the National Natural Science Foundation of China (Nos. 51802089, 52221001, 62090035, 62501489), the Natural Science Foundation of Hebei Province (E2024201020), Basic Research Program of Jiangsu Province (BK20250465), Nanjing MKNANO Tech. Co., Ltd. (www.mukenano.com), and the Ultra-Multi-Wavelength LED Sources (UMW-60) of Qingdao Solar Scientific Instrument High-tech Co., LTD.

Competing Interest Statement

The authors declare no competing interests.

References

1. Mennel L, Symonowicz J, Wachter S et al. Ultrafast machine vision with 2D material neural network image sensors. *Nature* 2020; **579**: 62-66.
2. Sangwan VK and Hersam MC. Neuromorphic nanoelectronic materials. *Nat. Nanotechnol.* 2020; **15**: 517-528.
3. Chai Y. In-sensor computing for machine vision. *Nature* 2020; **579**: 32-33.
4. Long Z, Zhou Y, Ding Y et al. Biomimetic optoelectronics with nanomaterials for artificial vision. *Nat. Rev. Mater.* 2024; **10**: 128-146.
5. Jiang M, Zhao Y, Liu T et al. A dual-mode transparent device for 360° quasi-omnidirectional self-driven photodetection and efficient ultralow-power neuromorphic computing. *Light: Sci. Appl.* 2025; **14**: 273.
6. Li C, Wang Y, Jiang Y et al. Ultrafast and stable flash memory with metal nanocrystals for logic-in-memory computing. *National Science Open* 2025; **4**: 20250059.
7. Wang Y, Liao K, Zhang K et al. Reconfigurable versatile integrated photonic computing chip. *eLight* 2025; **5:** 20.
8. Sun Z, Martinez A, and Wang F. Optical modulators with 2D layered materials. *Nat. Photonics* 2016, **10**: 227-238.
9. Liu J, Li B, Liu C et al. Devices, Functions, and Applications of Artificial Neuromorphic Visual Systems. *Adv. Sci.* 2025; **12:** 2516379.
10. Liu Y, Duan X, Shin HJ et al. Promises and prospects of two-dimensional transistors. *Nature* 2021; **591**: 43-53.
11. Liu C, Chen H, Wang S et al. Two-dimensional materials for next-generation computing technologies. *Nat. Nanotechnol.* 2020; **15**: 545-557.
12. Jiang J, Xiong M, Fan K et al. Synergistic strain engineering of perovskite single crystals for highly stable and sensitive X-ray detectors with low-bias imaging and monitoring. *Nat. Photonics* 2022; **16**: 575-581.
13. Zhang H, Pfeifer L, Zakeeruddin SM et al. Tailoring passivators for highly efficient and stable perovskite solar cells. *Nat. Rev. Chem.* 2023; **7**: 632-652.
14. Lin X, Chen L, He C et al. Vapor Phase Growth of Centimeter-Sized Band Gap Engineered Cesium Lead Halide Perovskite Single-Crystal Thin Films with

Color-tunable Stimulated Emission. *Adv. Funct. Mater.* 2022; **33**: 2210278.
15. Sun H, Li C, Li, L et al. The development of customized perovskite photodetectors. *Nat. Electron.* 2025; **8:** 1170-1181.
16. Qiao B, Wang S, Zhang Z et al. Photosensitive Dielectric 2D Perovskite Based Photodetector for Dual Wavelength Demultiplexing. *Adv. Mater.* 2023; **35**: 2300623.
17. Tang Y, Jin P, Wang Y et al. Enabling low-drift flexible perovskite photodetectors by electrical modulation for wearable health monitoring and weak light imaging. *Nat. Commun.* 2023; **14**: 4961.
18. Guo B, Lai R, Jiang S et al. Ultrastable near-infrared perovskite light-emitting diodes. *Nat. Photonics* 2022; **16**: 637-643.
19. Zhao B, Vasilopoulou M, Fakharuddin A et al. Light management for perovskite light-emitting diodes. *Nat. Nanotechnol.* 2023; **18**: 981-992.
20. Shi Y, Deng X, Gan Y et al. Ten Years of Perovskite Lasers. *Adv. Mater.* 2025; **37**: 2413559.
21. Liang J, Wang C, Wang Y et al. All-Inorganic Perovskite Solar Cells. *J. Am. Chem. Soc.* 2016; **138**: 15829-15832.
22. Sun X, Zhang P, Liu T et al. Surface Halide Manipulation for Stable Inorganic Perovskite Solar Cells and Modules. *Angew. Chem. Int. Ed.* 2025; **64**: 202501164.
23. Sutton RJ, Filip MR, Haghighirad AA et al. Cubic or Orthorhombic? Revealing the Crystal Structure of Metastable Black-Phase $CsPbI_3$ by Theory and Experiment. *ACS Energy Lett.* 2018; **3**: 1787-1794.
24. Li T, Xu J, Lin R et al. Inorganic wide-bandgap perovskite subcells with dipole bridge for all-perovskite tandems. *Nat. Energy* 2023; **8**: 610-620.
25. Ma Y, Wang Y, Fang Y et al. Recent Advances in the A-Site Cation Engineering of Lead Halide Perovskites. *Adv. Opt. Mater.* 2024; **12**: 2401367.
26. Li B, Mao W, Liang S et al. Blue perovskite single-mode lasing in a rubidium lead bromide microcubic cavity. *Photon. Res.* 2023; **11**: 1067.
27. Zhao P, Yin W, Kim M et al. Improved carriers injection capacity in perovskite solar cells by introducing A-site interstitial defects. *J. Mater. Chem. A.* 2017; **5**: 7905-7911.
28. Son DY, Kim SG, Seo JY et al.Universal Approach toward Hysteresis-Free Perovskite Solar Cell via Defect Engineering. *J. Am. Chem. Soc.* 2018; **140**: 1358-1364.
29. Wang Z, Zeng L, Zhu T et al. Suppressed phase segregation for triple-junction perovskite solar cells. *Nature* 2023; **618**: 74-79.
30. WHITE S, Ionic diffusion in quartz. *Nature* 1970; **225**: 375-376.
31. Li M, Luo J, He J et al. Bandgap Engineering Based on A-site Ions Tuning in Tin Halide Perovskite. *Small* 2025; **21**: 2409546.
32. Cao Y, Wang Q, Ji Z et al. Mechanisms of Enhanced Efficiency and Stability in Perovskite Luminescence via Rb Interstitial Doping. *J. Phys. Chem. Lett.* 2025; **16**: 9664-9671.
33. Yang Z, Lin CQ, and Pan CY. Rb and Cl co-doped $CsPbBr_3$ QDs for bright blue light emitting diode. *J. Solid State Chem.* 2025; **343:** 125164.

34. Sun R, Jia Y, Lai B et al. Phase-pure ferroelectric quantum wells with tunable photoluminescence for multi-state optoelectronic applications. *Light: Sci. Appl.* 2025; **14**: 228.
35. Xiao J, Yuan L, Zhang S et al. Stabilizing $RbPbBr_3$ Perovskite Nanocrystals through Cs^+ Substitution. *Chem. Eur. J.* 2019; **25**: 2597-2603.
36. Zheng W, Jiang Y, Zheng B et al. Direct Synthesis of Atomically Smooth Epitaxial PbI_2 Nanosheets for Low-Threshold Monolithic Spin Lasers. *J. Am. Chem. Soc.* 2025; **147**: 42123-42132.
37. He J, Luo J, Zheng B et al. General phase segregation and phase pinning effects in lanthanide-doped lead halide perovskite with dual-wavelength lasing. *Nat. Commun.* 2025; **16**: 11161.
38. Rong K, Duan X, Wang B wt al. Spin-valley Rashba monolayer laser. *Nat. Mater.* 2023; **22**: 1085-1093.
39. Li Y, Zhang J, Huang D et al. Room-temperature continuous-wave lasing from monolayer molybdenum ditelluride integrated with a silicon nanobeam cavity. *Nat. Nanotechnol.* 2017; **12**: 987-992.
40. Ye Y, Wong ZJ, Lu X et al. Monolayer excitonic laser. *Nat. Photonics* 2015; **9**: 733-737.
41. Fu Y, Zheng W, Wang X et al. Multicolor Heterostructures of Two-Dimensional Layered Halide Perovskites that Show Interlayer Energy Transfer. *J. Am. Chem. Soc.* 2018; **140**: 15675-15683.
42. Qiu H, Li F, He S et al. Epitaxial $CsPbBr_3$/CdS Janus nanocrystal heterostructures for efficient charge separation. *Adv. Sci.* 2023; **10**: 2206560.
43. Wu F, Li Q, Wang P et al. High efficiency and fast van der Waals hetero-photodiodes with a unilateral depletion region. *Nat. Commun.* 2019; **10**: 4663.
44. Tayari V, Hemsworth N, Fakih I et al. Two-dimensional magnetotransport in a black phosphorus naked quantum well. *Nat. Commun.* 2015; **6**: 7702.
45. Gao J, Li B, Tan J et al. Aging of Transition Metal Dichalcogenide Monolayers. *ACS Nano* 2016; **10**: 2628-2635.
46. Tong B, Xu J, Du J et al. 2D $(NH_4)BiI_3$ enables non-volatile optoelectronic memories for machine learning. *Nat. Commun*. 2025; **16**: 1609.
47. Li H, Liu J, Geng S et al. A 2D-3D Perovskite Memristor-Based Light-Induced Sensitized Neuron for Visual Information Processing. *Adv. Mater.* 2025; **37**: 2408342.
48. Liu K, Zhang T, Dang B et al. An optoelectronic synapse based on α-In_2Se_3 with controllable temporal dynamics for multimode and multiscale reservoir computing. *Nat. Electron.* 2022; **5**: 761-773.
49. Wang B, Zhang X, Wang S et al. Topology optimization of random memristors for input-aware dynamic SNN. *Sci. Adv.* 2025; **11**: eads5340.

Figures and Tables

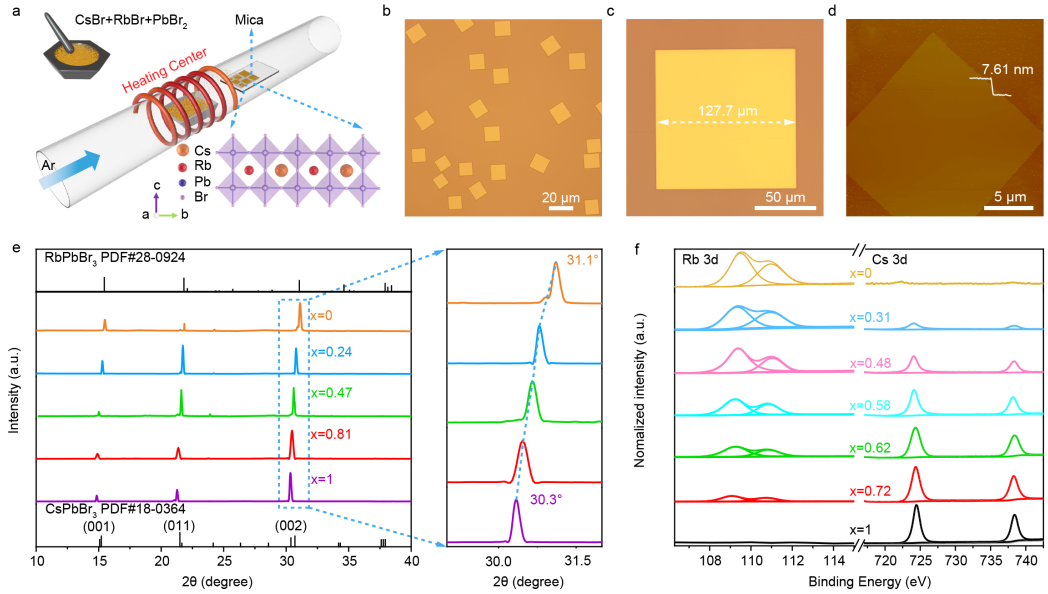

Figure 1. (a) Growth illustration of $Cs_xRb_{1-x}PbBr_3$ ($0 \le x \le 1$) nanosheets. (b) Typical optical image of the as-grown $Cs_xRb_{1-x}PbBr_3$ ($0 \le x \le 1$) nanosheets on mica substrate. (c) OM image of a representative $Cs_xRb_{1-x}PbBr_3$ ($0 \le x \le 1$) nanosheet with lateral size ≈ 127.7 μm. (d) AFM image and thickness information of a $Cs_xRb_{1-x}PbBr_3$ ($0 \le x \le 1$) nanosheet. (e) XRD patterns of $Cs_xRb_{1-x}PbBr_3$ (x = 1, 0.81, 0.47, 0.24, 0). (f) Cs 3d and Rb 3d core level XPS spectra.

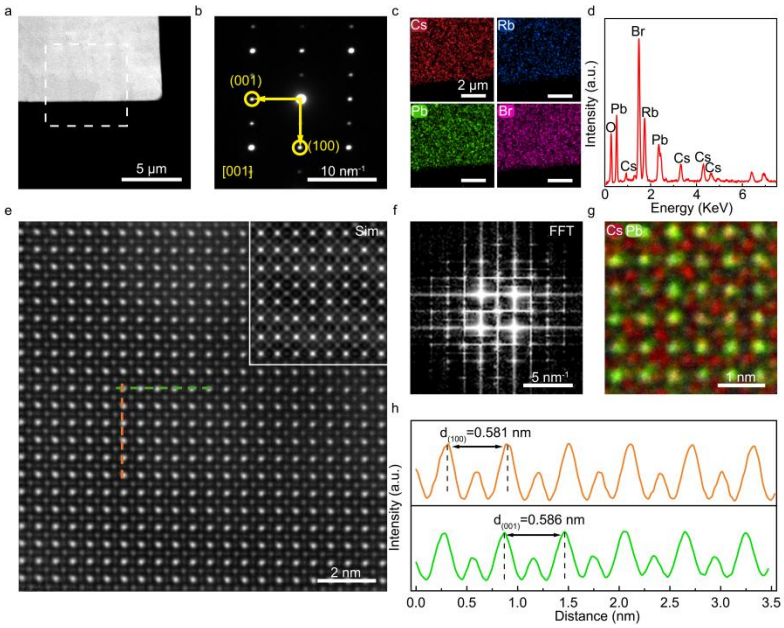

Figure 2. (a, b) Low-magnification HAADF-STEM and SAED images of a representative $Cs_xRb_{1-x}PbBr_3$ nanosheet. (c) EDS mapping of the elements Cs, Rb, Pb, and Br in the white box of (a). (d) EDS spectrum of the $Cs_xRb_{1-x}PbBr_3$ nanosheet. (e) Atomic-resolution HAADF-STEM image of a typical $Cs_xRb_{1-x}PbBr_3$ nanosheet, inset: simulative image of the crystal. (f) FFT diffraction spots of (e). (g) Atomic-resolution EDS elemental mapping of Cs (red) and Pb (green). (h) Intensity profile along the orange and green dashed lines in (e).

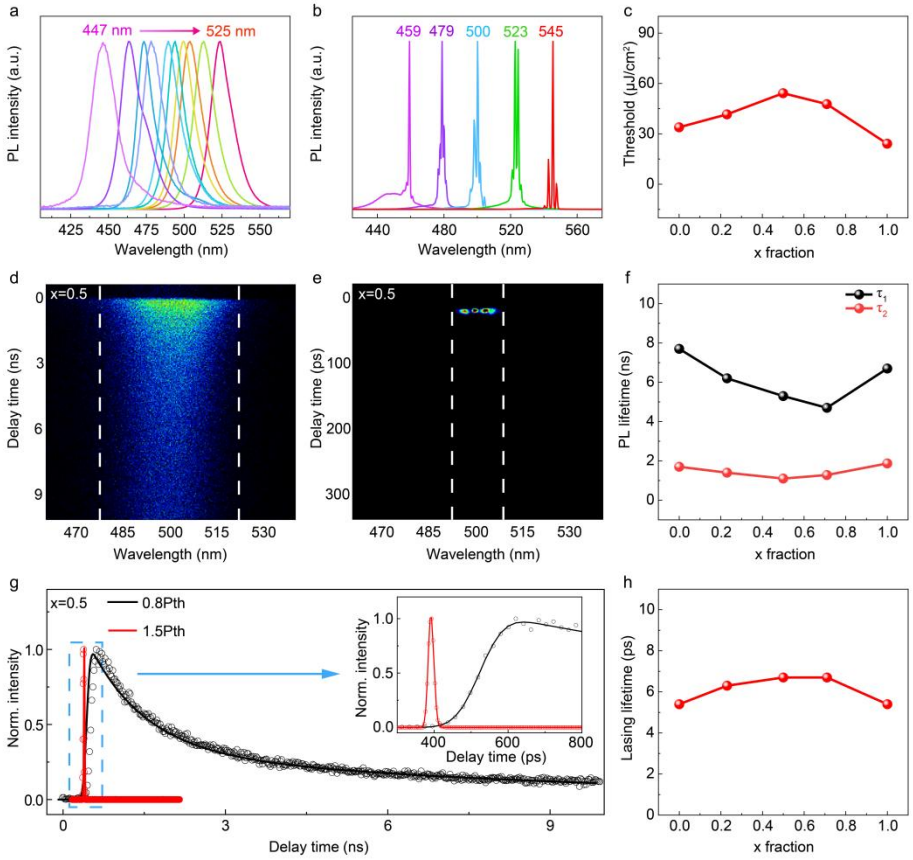

Figure 3. (a) PL spectra of $Cs_xRb_{1-x}PbBr_3$ ($0 \le x \le 1$) nanosheets. (b) The emission spectra of $Cs_xRb_{1-x}PbBr_3$ ($0 \le x \le 1$) nanosheets. (c) Lasing thresholds extracted from the selected in (b). Streak-camera images of a $Cs_{0.5}Rb_{0.5}PbBr_3$ nanosheet recorded under excitation power of (d) 0.8 P_{th} (threshold excitation power) and (e) 1.5 P_{th}. (f) Fitting parameters for the PL decay curves in (b). (g) Typical PL-decay curve obtained at two different excitation powers (0.8, 1.5 P_{th}). (h) Fitting parameters for the Lasing decay curves of the representative alloyed compositions.

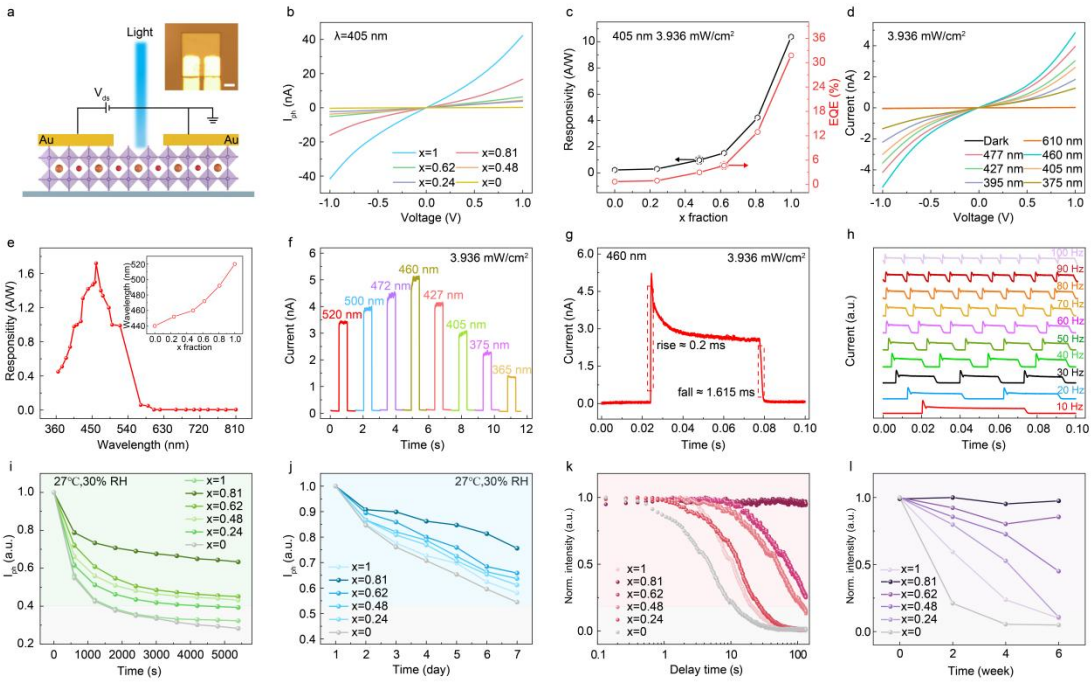

Figure 4. (a) Schematic illustration of an individual nanosheet-based PD. Inset: OM image of a typical device (Scale bar: 10 μm). (b) Composition-dependent I-V characteristics measured under 405 nm illumination (3.936 mW/cm^2). (c) R and EQE as a function of fraction (x). (d) Wavelength-dependent I-V curves of the $Cs_{0.48}Rb_{0.52}PbBr_3$ device. (e) Wavelength-dependent R at 1 V bias. Inset: The peak sensitivity wavelength of the alloy as a function of the atomic percentage of component x. (f) Rise and fall time of the $Cs_{0.48}Rb_{0.52}PbBr_3$ PD measured under 1 V. (g) Variable frequency-dependent transient photoresponse curves of $Cs_{0.48}Rb_{0.52}PbBr_3$ PD with frequency at 1V. (h) The I-T curves under periodic illumination at different wavelengths with a 1 V bias. (i) Time stability of devices at same humidity level of $Cs_xRb_{1-x}PbBr_3$ ($0 \le x \le 1$) nanosheets PDs. (j) Long-term environmental stability of the photodetector devices (monitored via photocurrent I_{ph}) stored in air (27℃, 30% RH) for 7 days. (k) Normalized PL intensity evolution of the alloyed nanosheets as a function of delay time. (l) Long-term optical stability of $Cs_xRb_{1-x}PbBr_3$ ($0 \le x \le 1$) nanosheets, characterized by the evolution of normalized PL intensity over six weeks.

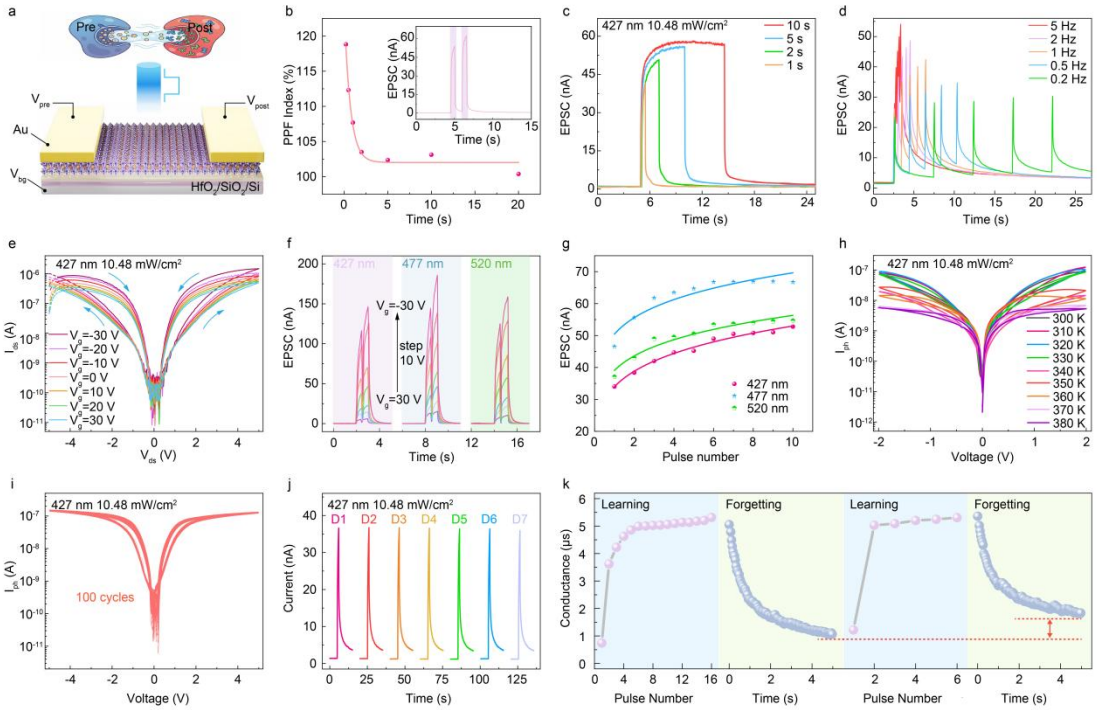

Figure 5. (a) Schematic illustration of the photosynapse device. (b) PPF ratio as a function of pulse interval; the red curve represents a double-exponential fit. Synaptic responses under 427 nm illumination with varying (c) pulse width and (d) pulse frequency. (e) I-V curves under different back-gate voltages. (f) Photoresponses under different back-gate voltages. (g) Synaptic responses to optical stimuli with different wavelengths and pulse numbers. (h) Switching behavior under elevated temperatures. (i) Endurance performance over repeated optical stimulation cycles. (j) Photoresponse stability of device cover with PMMA after storage in ambient air for 7 days. (k) Learning-forgetting-relearning behavior emulated by the device.

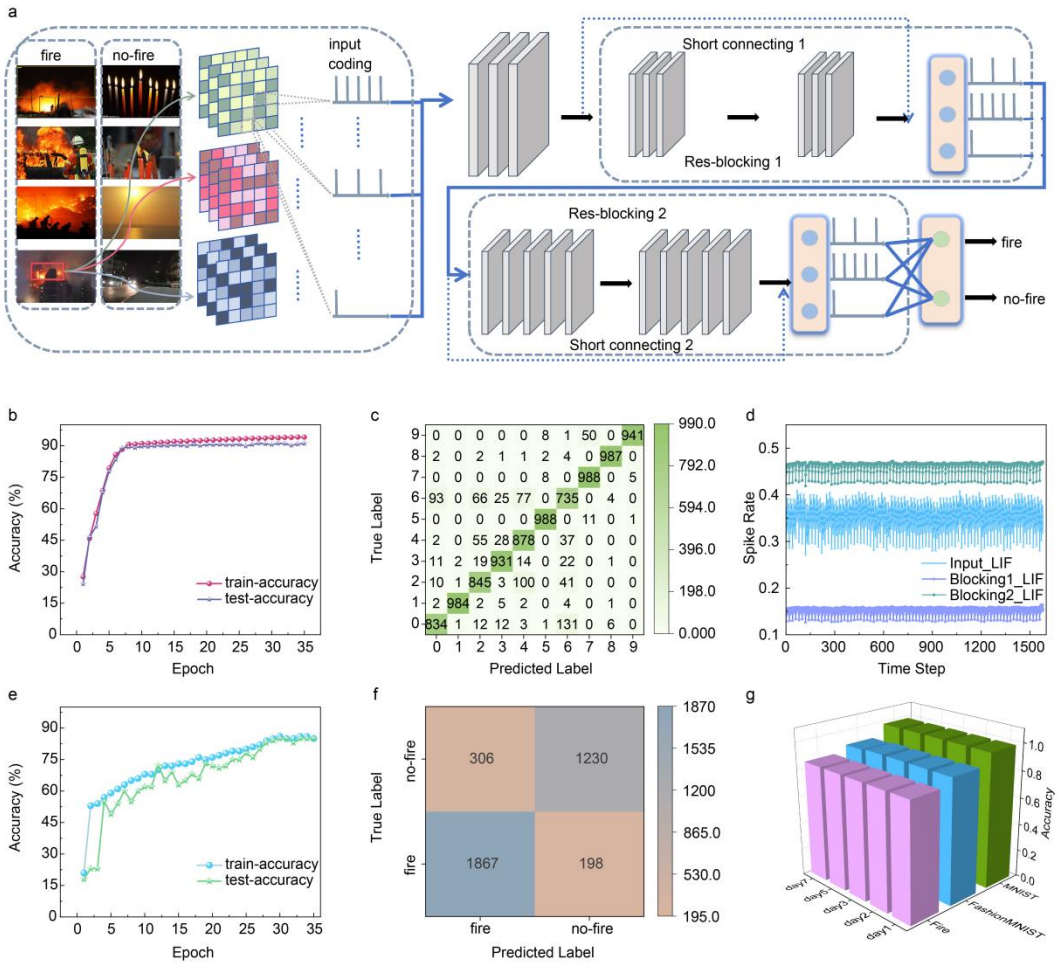

Figure 6. (a) Architecture of the ResNet-SNN used for image classification. (b) Training and inference accuracy on the FashionMNIST dataset. (c) Confusion matrix after final training on FashionMNIST. (d) Firing frequency distribution of LIF neurons. (e) Training and inference accuracy on the fire dataset. (f) Confusion matrix for fire detection. (g) Evolution of inference accuracy over extended operation time.

TOC Figure

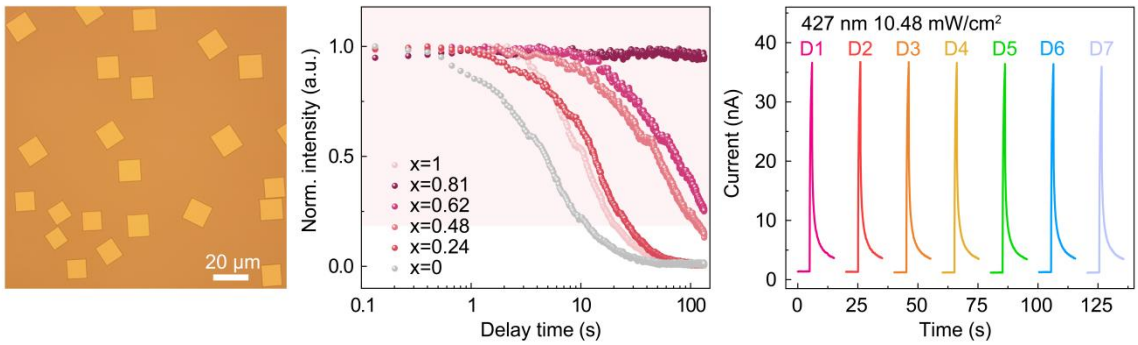
20 μm
Norm. intensity (a.u.)
1.0
0.5
0.0
x=1
x=0.81
x=0.62
x=0.48
x=0.24
x=0
0.1
1
10
100
Delay time (s)
427 nm 10.48 mW/cm²
D1
D2
D3
D4
D5
D6
D7
Current (nA)
40
30
20
10
0
0
25
50
75
100
125
Time (s)